Journal of Manufacturing Processes 101 (2023) 1508–1520

Contents lists available at ScienceDirect

Journal of Manufacturing Processes

journal homepage: www.elsevier.com/locate/manpro

Anisotropic sintering shrinkage behavior of stainless steel fabricated by extrusion-based metal additive manufacturing

Siyao You [a], Dayue Jiang [b], Fuji Wang [a], Fuda Ning [b,*]

[a] School of Mechanical Engineering, Dalian University of Technology, Dalian 116023, China
[b] Department of Systems Science and Industrial Engineering, State University of New York (SUNY) at Binghamton, Binghamton, NY 13902, USA

ARTICLE INFO

Keywords:
Additive manufacturing
Material extrusion
Sintering
Stainless steel 316 L
Anisotropic shrinkage

ABSTRACT

Metal additive manufacturing (AM) can be achieved by first extruding polymer-based filaments with densely filled metal particles to create the so-called 'green' parts and then experiencing debinding and sintering to produce finished metal components. As a critical step, sintering governs the shape dimension, relative density, and resultant strength of final parts. Thus, there is a growing need for research on understanding and quantifying the sintering-induced anisotropic shrinkage. In this work, the underlying behaviors of anisotropic shrinkage during the entire sintering of extrusion-printed stainless steel 316L parts will be understood and quantified through a combination of theoretical study and experimental investigations including three-directional dilatometry, scanning electron microscopy, and X-ray computed tomography. The three-dimensional size evolution of 'brown' parts before sintering will be studied through a macroscopic analysis of shrinkage anisotropy factors and microstructure characterizations. Different filling strategies will be integrated with initial pore distribution characterization for anisotropic dimensional change analysis. The heterogeneous pore distribution will be discussed in conjunction with the anisotropic viscous behavior to eventually unveil the shrinkage performance in the course of sintering. The findings of this work will provide insights into the anisotropic sintering mechanisms and fill the knowledge gap of the relations between extrusion-based metal AM process and sintered structures of metal alloys.

1. Introduction

Material extrusion (ME) additive manufacturing (AM) process has become a relatively new AM method for metal part fabrication. First, the polymer-based filaments with highly filled metal particles are used to print the 'green' part, in which the polymetric binder will then be removed via the solvent, catalytic, or thermal debinding to form a 'brown' part. The final dense metal parts can be achieved through a subsequent high-temperature sintering process. Such a multi-step approach is defined as extrusion-based printing-debinding-sintering (PDS) process in this work. Compared with other metal AM technologies, PDS features ease of part handling and reduction of production costs, favoring the scalable manufacturing and rapid fabrication of metal components at relatively high manufacturing efficiency [1].

Sintering plays a crucial role in determining the density, microstructure, and the resultant mechanical properties of the finished parts [2]. Early studies have indicated a significant anisotropic shrinkage phenomenon after metal/ceramic sintering [3,4]. For porous powder compacts, anisotropic shrinkage can originate from two sources [5]: (1) anisotropic microstructure (e.g., preferential orientation of anisometric particles [6–8], uneven particle size [9], non-uniform crystallographic texture and orientation [10–12], irregular pore shape [13], porosity [14], uneven initial density distribution and multilayered/laminated structures [15–18]) in 'green' parts; and (2) external fields (e.g., stress, gravity, and thermal gradient [19–21]) that may lead to larger deformation in the direction of the applied field. By measuring the ratio of axial and radial dimensions after sintering, we can quantify the anisotropic shrinkage behavior [22]. During the sintering process, the dimensional control of final metal parts requires a thorough analysis of the associated anisotropy to achieve highly precise components, which emphasizes the urgent need for understanding and predicting the anisotropic sintering behavior.

At present, experiments have been conducted to study the anisotropic sintering shrinkage phenomenon of PDS-built metals, indicating a larger shrinkage along the Z direction than the other two. For example, the PDS-built stainless steel (SS) 316L exhibited a shrinkage of 17.5 %

* Corresponding author.
E-mail address: fning@binghamton.edu (F. Ning).

https://doi.org/10.1016/j.jmapro.2023.07.026
Received 16 May 2023; Received in revised form 12 July 2023; Accepted 12 July 2023

and 14.5 % along the building direction and in-plane direction, respectively [23]. The test results of 17–4 PH also confirmed the maximum shrinkage at the *Z*-axis [24]. Relevant literature results of sintering shrinkage are summarized in Table 1.

Such an anisotropic shrinking phenomenon is commonly explained by the interlayer defects caused at the printing stage [31]. Due to the inevitable layer-by-layer fabrication, the arranged particle accumulation results in the initial non-uniform density distribution in the 'brown' part. To alleviate the anisotropic shrinkage, efforts have been made to tailor the internal microstructures. He et al. claimed that the addition of the pore former can help to improve the pore interconnectivity and pore size of the 'green' parts [32]. The research results of Baumgartner et al. demonstrated that appropriate modifications to the model design in the CAD file can also control the three-directional shrinkage [33].

In addition to the experimental studies above, analytical modeling has been used to provide an in-depth understanding of the anisotropic shrinkage in sintered parts. The sintering stress and viscosity tensors have been linked to the shrinkage of porous materials [15]. Also, thermal elastic/viscoplastic constitutive models have been developed in the literature to predict the dimensional changes and densification of compressible porous components during sintering processes [34–37]. However, the governed isotropic sintering variables (e.g., strain rate tensor, stress tensor, viscous modulus, and sintering stress [38–40]) cannot accurately quantify the anisotropic shrinkage during the sintering in PDS. They are subject to particle morphology, porosity, specific surface energy, self-diffusion coefficient, particle arrangement, etc., thus posing a great challenge to elucidate the anisotropic sintering behavior in PDS. In our previous study [41], the anisotropic deformation of overhang structure after sintering was studied, showing that the shrinkage along the building direction is about 3 % higher than in-plane direction. However, multi-scale mechanism is involved in sintering shrinkage densification due to its complex thermodynamics that governs the microstructure morphology and macroscopic viscous behavior. Therefore, it is necessary to further explore the potential evolution of anisotropic sintering shrinkage in PDS.

In this work, we will understand and quantify the anisotropic shrinkage behavior and its relationship with the heterogeneous pore distribution during sintering of extrusion-printed SS 316L. First, the anisotropic dimensional evolution during the entire sintering stage is uncovered through a three-directional dilatometry test and microstructure characterization. Subsequently, internal pore structures of the pre-sintered 'brown' parts are quantified through X-ray computed tomography, which can further explain the anisotropic shrinkage behavior. Based on the established analytical model for the anisotropic sintering, we decipher the correlation between heterogeneous pore distribution and anisotropic viscous behavior by introducing the parameters relevant to the anisotropic viscosity. This work provides valuable insights into the sintering behavior of ME-printed anisotropic parts, advancing the understanding of the sintering process in PDS for other metal/ceramic materials.

2. Experimental conditions

2.1. Feedstock

The feedstock filament (Ultrafuse SS 316L, BASF, Ludwigshafen, Germany) applied in this study was comprised of around 88 wt% of metal particles and a polyformaldehyde (POM)-based binder system and had a diameter of 2.85 mm. The average diameter of 316L powder in the mixed filament was 6 μm [23]. In addition, a certain amount of additive mixture (polypropylene (PP), dioctyl phthalate (DOP), dibutyl phthalate (DBP), and zinc oxide (ZnO), etc.) was specifically added to improve the processability of the filament [42]. Fig. 1 displays the PDS process.

2.2. Printing and pre-sintering processes

The 'green' parts were printed on a desktop FFF printer (TAZ6, Lulzbot, Loveland, TX, USA). Table 2 gives the printing parameters. Subsequently, the printed 'green' parts were subjected to a gaseous nitric acid (HNO_3) atmosphere to complete catalytic debinding process at an outsourced oven under 120 °C (CD3045, Elnik Systems, Cedar Grove, Service Provider in USA), which could remove approximately 97 wt% of the binder system. The debound 'brown' part is extremely fragile at this time. Although the 3 wt% residual backbone polymer provides some level of support, physical bonding between the metal particles still causes a potential risk of collapsing and excessive sintering deformation [43]. The highly temperature-dependent atomic diffusion is accompanied by the gasification of residual polymers, inducing crack generation. Therefore, the pre-sintering process performed before dilatometry tests become particularly important.

Thermogravimetric analysis (TGA) (TG 209 F3 Tarsus, Selb, Germany) was conducted on the filament under a nitrogen atmosphere to determine the final pre-sintering profile, as shown in Fig. 2(a). The milled filament powder was heated to 973 K at a rate of 5 K/min. The curve demonstrates that the primary binder in the filament begins to decompose at 588 K and reaches a mass loss of nearly 11 % at up to 693 K, which corresponds to the removal of most of the binder after catalytic debinding. Subsequently, the mass losses at about 723 K and 873 K may represent the degradation of residual polymer backbones. The commonly used pre-sintering peak temperature of SS 316L after debinding is 1173 K [45]. The developed pre-sintering temperature profile is exhibited in Fig. 2(b). Then, the weight and dimensions of pre-sintered 'brown' parts were measured, and the relative density of the pre-sintered 'brown' parts was calculated.

2.3. Dilatometry test

To determine the anisotropic sintering densification behavior, dilatometry test was conducted on three pre-sintered cubic specimens with a dimension of 6.35 × 6.35 × 6.35 mm^3. Pure hydrogen atmosphere was applied in a horizontal dilatometry (TA instruments, Theta 1600, New Castle, USA) to densify the pre-sintered 'brown' parts. Fig. 4 shows the temperature evolution through the whole dilatometry test. The heating involved a 5 K/min heating ramp to 1653 K and 3 h of holding. To capture instantaneous shrinkages of 'brown' parts in three directions

Table 1
Summary of the shrinkage of PDS-built stainless steel parts in the literature.

Material	Sintering conditions	X-axis shrinkage	Y-axis shrinkage	*Z*-axis shrinkage	Relative density	Literature
316L	1280 °C/Ar	14–15 %	14–15 %	15–17 %	92.9 %	[3]
	1380 °C/H_2	14–18 %	14–18 %	18–23 %	98.5 %	[25]
	1360 °C/N_2	16.4 %	16.4 %	20 %	>97 %	[26]
	1380 °C/H_2	15.31–15.48 %	15.16–16.37 %	17.26–17.80 %	88.55 %	[27]
	1380 °C/H_2	15.5 %–20.4 %	15.5 %–20.4 %	18.5 %–23.1 %	95 %	[28]
	1380 °C/H_2	13 %–18 %	13 %–18 %	15 %–23 %	95.4 %	[29]
17–4 PH	1380 °C/H_2	15.9 %	15.2 %	20.3 %	96 %	[24]
	1280 °C/Ar	15.1 %	15.3 %	16.8 %	97.5–98 %	[30]

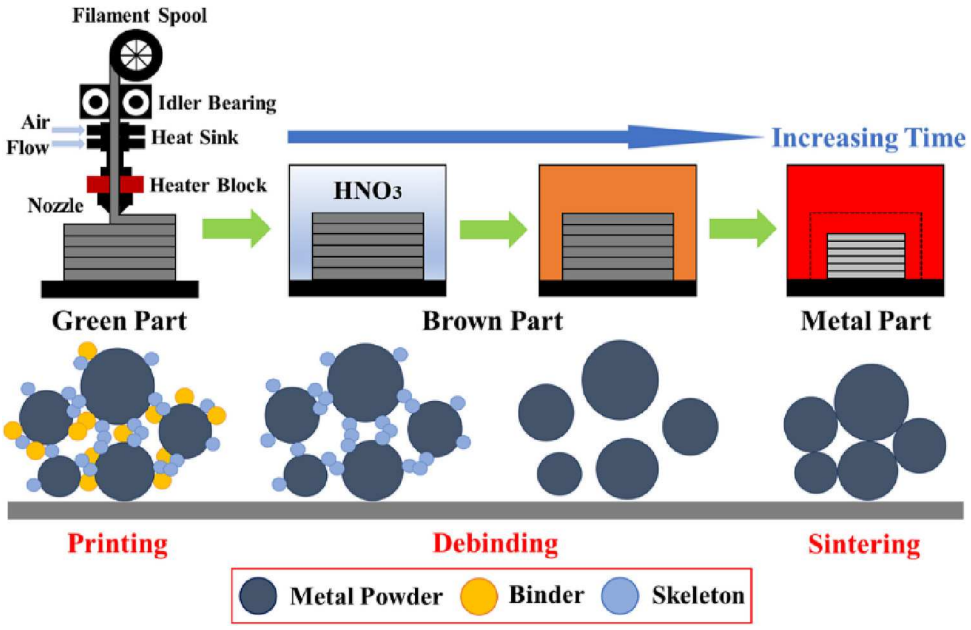

Fig. 1. Schematic diagram of printing-debinding-sintering (PDS) process.

Table 2
Printing parameters for FFF process.

Printing parameters	Values
Nozzle temperature	240 °C
Nozzle diameter	0.5 mm
Infill density	100 %
Filling strategy	Alternating 45°
Printing speed	30 mm/s
Layer thickness	0.2 mm
Bed temperature	100 °C

during the sintering, we used X-axis as the horizontal reference direction and rotated Y and Z directions to this direction, respectively (see Fig. 3). These data were processed and analyzed in the Section 4.1, in conjunction with the relative density data of pre-sintered 'brown' parts.

2.4. Sintering

Different from those in the dilatometry test above, the parts experienced a couple of holding stages at temperatures of 723 K, 873 K, 1323 K, and 1653 K, respectively, during thermal debinding and sintering processes in an outsourced furnace (MIM 3045, Elnik Systems, Cedar Grove, Service Provider in USA), as illustrated in Fig. 5. The ramp rate was 5 K/min, and the sintered metal parts were air-cooled to room temperature to complete sintering.

2.5. Microstructure characterization

The microstructures of SS 316L specimens at various PDS stages, including printed 'green' part, debound 'brown' part, and sintered metal part, were characterized by scanning electron microscopy (SEM, Supra 55 VP, Zeiss Corp., Germany). The phase distribution and grain orientation mapping of sintered SS 316L specimen after mechanical grinding and electropolishing were conducted using an electron backscattered diffraction (EBSD) analyzer (Hikari Plus, EDAX Corp., USA) with a step size of 500 μm.

2.6. X-ray computed tomography

3D morphology of the pores in the 'brown' parts was quantified by X-ray computed tomography (CT) platform (V Tome XS240, GE Phoenix X-ray, Germany) with a spatial resolution of 10 μm. Binarized segmentation was conducted based on the grayscale images of the 2D slice obtained by the scanned pre-sintered 'brown' parts, and 3D volume rendering was performed using the data analysis/visualization software

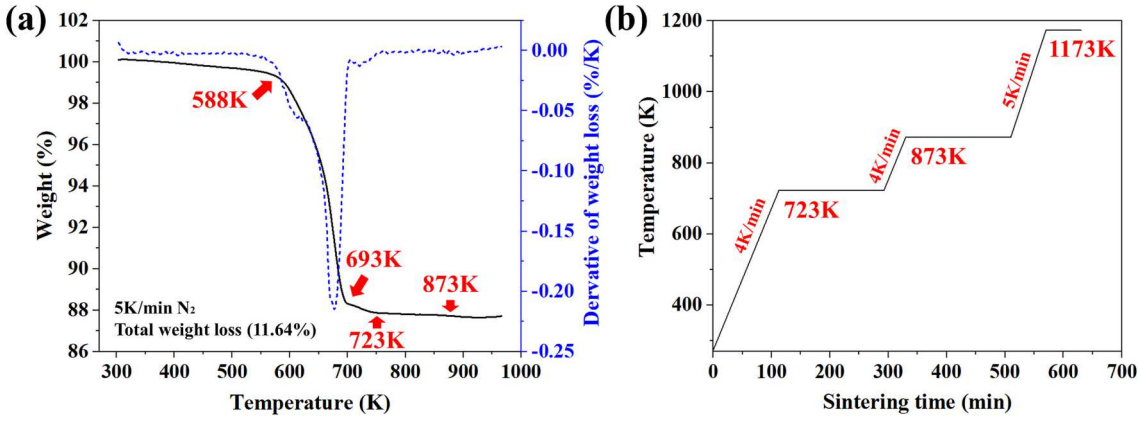

Fig. 2. **(a)** Thermogravimetric analysis (TGA) of Ultrafuse SS 316 L filament, **(b)** pre-sintering heating curve.

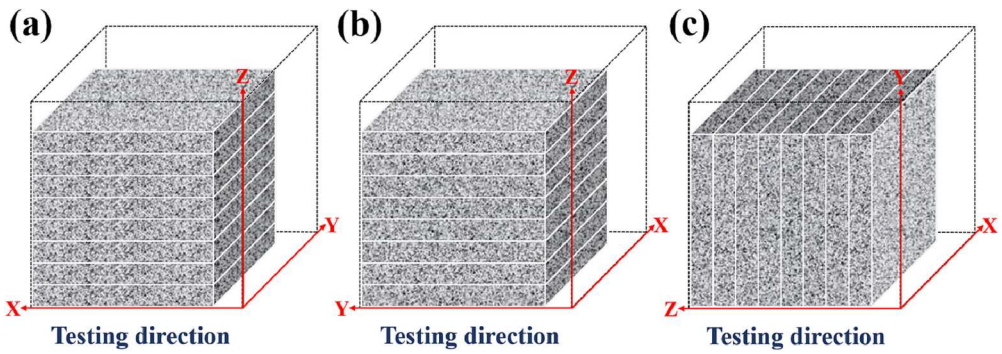

Fig. 3. Measurement method for anisotropic sintering shrinkage.

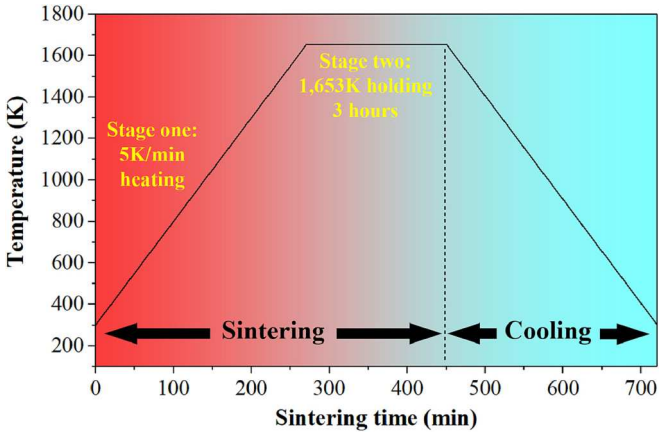

Fig. 4. Temperature evolution of the pre-sintered 'brown' part during the entire dilatometry test.

(VG Studio Max).

3. Theoretical modeling

Based on the constitutive model describing the viscous sintering process of a porous continuum, our previous work has successfully predicted the sintering deformation behavior of overhang structures after PDS sintering [41]. Based on the dilatometry data along X, Y, and Z directions and identified parameters including anisotropic viscosity activation energies (Qx, Qy, and Qz), grain radius r, temperature T, shear modulus φ, and bulk modulus ψ, the evolution process of anisotropic shrinkage behavior in PDS was deeply deciphered.

Specifically, anisotropic pre-exponential factor ratios (η_{0x}/α, η_{0y}/α, and η_{0z}/α) in the developed constitutive model [41] were reextracted, respectively. Regression equations were used to obtain their relationships with porosity θ, for the purpose of quantifying the formation and attenuation of three-directional viscous behaviors in the anisotropic shrinkage phenomenon. The flowchart in Fig. 6 presents an overview of the anisotropic η_0/α extraction and regression processes.

4. Results and discussion

In this section, the anisotropic shrinkage process during PDS will be analyzed based on the dilatometry test result. Subsequently, the pore distribution dependent anisotropic shrinkage behavior will be elucidated based on the quantitative analysis of internal pores during sintering with variable filling strategies. Finally, anisotropic viscosity will be introduced to further explain the formation of this anisotropic shrinkage.

4.1. Anisotropic shrinkage during PDS

Fig. 7 depicts the results of the dilatometry experiments in three directions, based on which we will establish the relationship between anisotropic strain rates and porosity evolution. In detail, e is the true logarithmic strain, which is converted from the dilatometry data of the

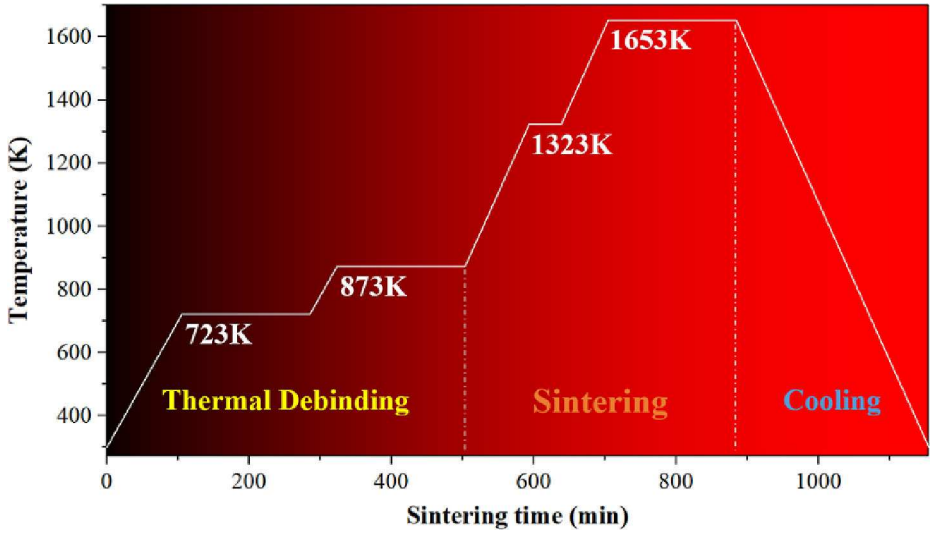

Fig. 5. Sintering temperature profile of SS 316L part (provided by DSH Technologies).

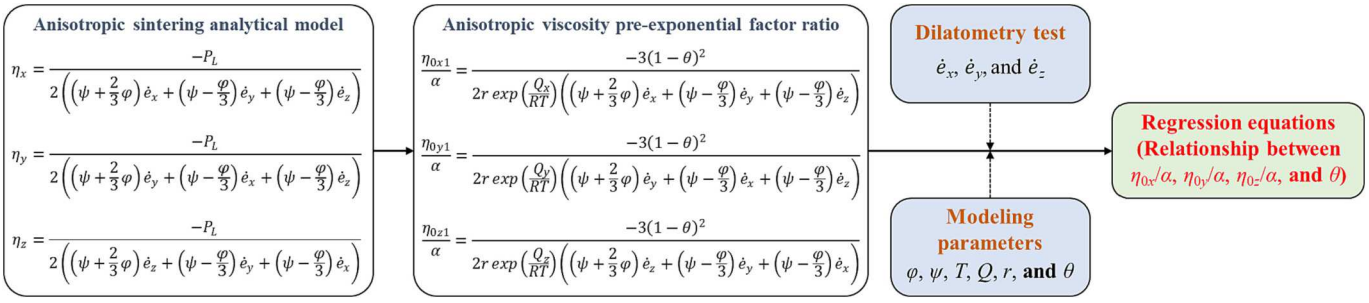

Fig. 6. The main procedures of theoretical model development.

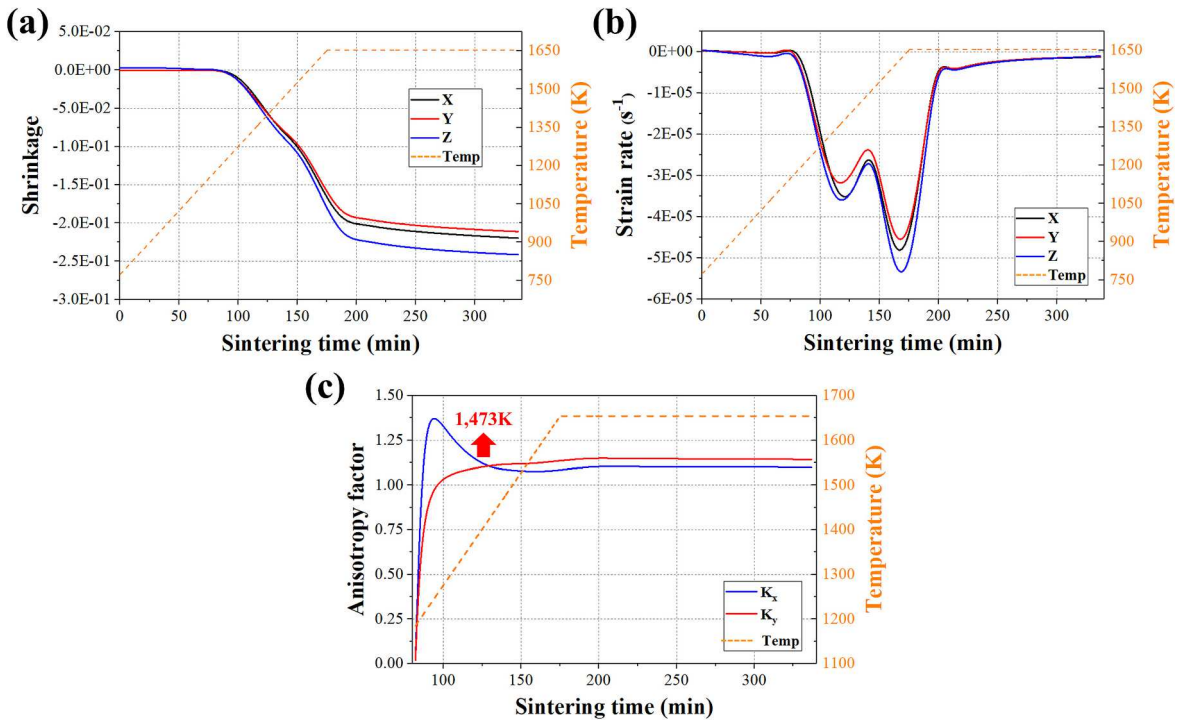

Fig. 7. **(a)** Three-dimensional strain-time curves during sintering, **(b)** calculated corresponding logarithmic strain rates, and **(c)** the evolution of anisotropic factors (K_x and K_y) during sintering, as calculated from dilatometry data in panel (a).

engineering strain (actual size shrinkage) by the following equations:

$$e = ln(1+\lambda) = ln\left(1+\frac{l_n - l_0}{l_0}\right) = ln\left(\frac{l_n}{l_0}\right) \tag{1}$$

$$\dot{e} = \frac{de}{dt} \tag{2}$$

where λ is engineering strain, l_0 is the initial length of the specimen, and l_n is the instantaneous length of the specimen. It can be indicated from displacement and strain rate curves in Fig. 7(a) and (b) that the pre-sintered 'brown' parts exhibit anisotropic shrinkage behaviors during the sintering. Specifically, the size shrinkage and strain rate suggest that there are no significant differences in magnitudes of curves below 1473 K. Compared to X and Y directions, the size shrinkage and strain rate are larger along the building direction (*Z*-axis) when the temperature exceeds 1473 K. Then, strain rate curves of these three directions present a trend to stabilize gradually at the final stage of the sintering process. This indicates the shrinkage behavior tends to become isotropic when the sintering process is completed.

To quantify the dynamic evolution of anisotropic shrinkage with sintering temperature and time, the shrinkage anisotropy factors [31], $K_x = \lambda_z/\lambda_x$ and $K_y = \lambda_z/\lambda_y$ throughout the sintering process, are calculated using three-dimensional data from dilatometry tests, as shown in Fig. 7(c). Earlier sintering data (below 1100 K) is removed to exclude the effect of thermal expansion. The larger difference in the curves at low temperature indicates that the three-directional shrinkage conditions of the specimen are completely different from that in the later sintering process. Specifically, the specimen exhibits the lowest strain rate along the Y direction below 1473 K, as shown in Fig. 7(b). The non-stationary random fluctuations in Fig. 7(c) could be due to an inherent error in the three-directional dilatometry test. And then, it is noted that the intersection of the two curves is 1473 K, and then tends to 1, and the final average factors for both are K_x = 1.1102 and K_y = 1.1068. Therefore, it can be suggested that 1473 K is the critical temperature point at which the sintering shrinkage behavior begins to transform from anisotropy to isotropy.

As another important sintering parameter, the porosity θ and geometrical relative density ρ can be determined in terms of the logarithmic strain rates along all directions through the mass conservation equation [46]. The density of the pre-sintered part is measured to be 4.34 g/cm^3, which represents a relative density of 0.54.

$$\frac{\dot{\theta}}{1-\theta} = \dot{e}_x + \dot{e}_y + \dot{e}_z \tag{3}$$

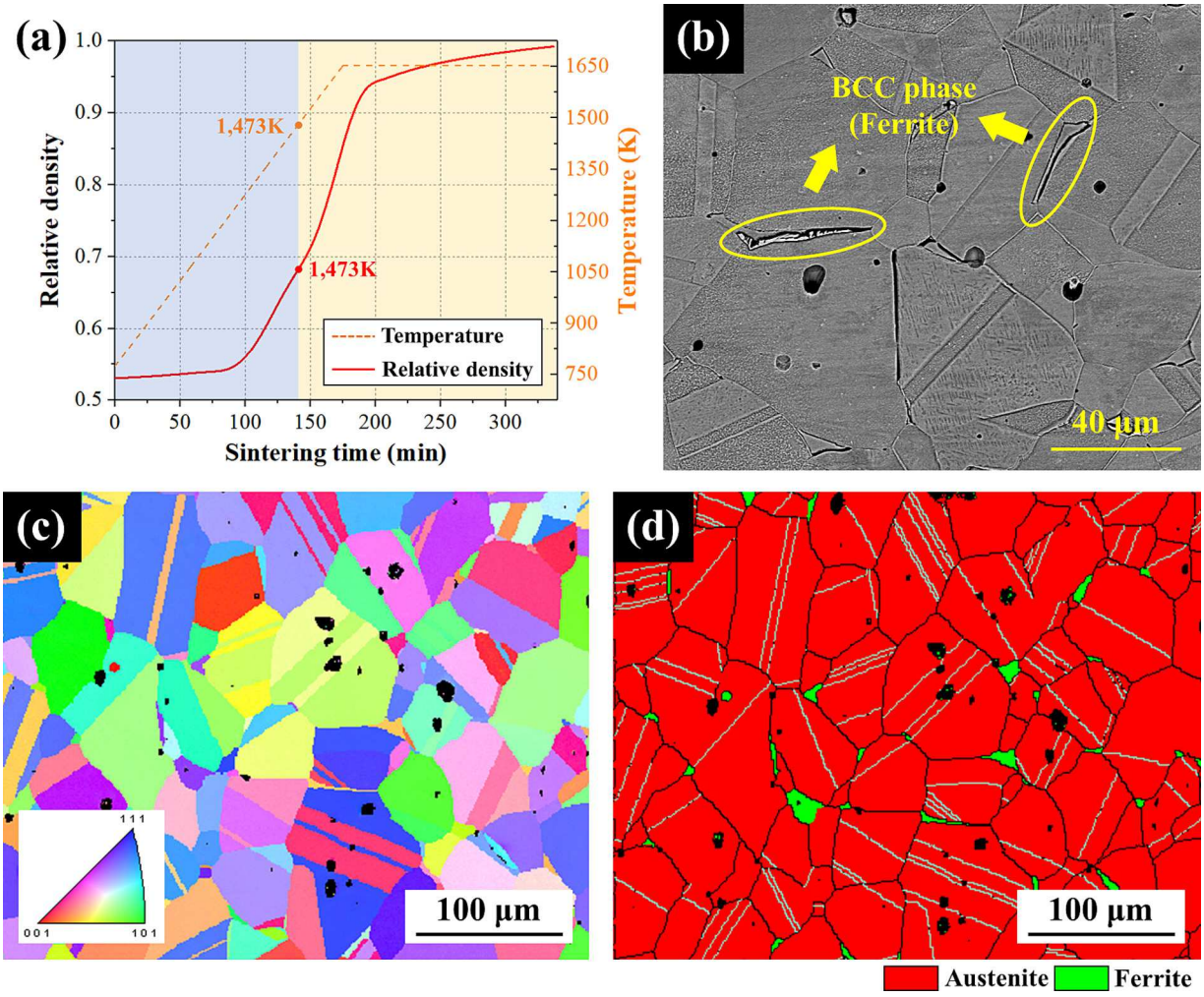

Fig. 8. **(a)** The evolution of relative density with sintering time and temperature, and the microstructure of SS 316L cube specimen after dilatometry test: **(b)** SEM image, **(c)** EBSD grain orientation, and **(d)** EBSD phase distribution.

$$\rho = 1 - \theta \tag{4}$$

The densification curve in Fig. 8(a) indicates that sintering begins at 1173 K and terminates at approximately 1653 K holding stage. It is also worth noting the abrupt acceleration in densification process at 1473 K is associated with the second increase in strain rates at this time, which shows great differences from conventional sintering phenomena. It was reported that enhanced densification could also be caused by the formation of body centered cubic phase (δ-ferrite) at high temperature, which has a higher self-diffusion rate than the austenitic matrix [31]. SEM and EBSD results in Fig. 8(b) and (d) also confirm many δ-ferrite meshes penetrating austenite grain boundaries. Related studies show that the δ-ferrite phase has begun to form above 1473 K [47]. During the final sintering stage (1653 K holding), the reduction of diffusion pathway caused by grain growth makes the sintering shrinkage rate slow down greatly [31]. Therefore, the further acceleration of the sintering shrinkage process after 1473 K could also be related to the formation of δ-ferrite. However, no clear correlation was found between δ-ferrite formation and anisotropic shrinkage.

4.2. Relationship between anisotropic shrinkage and heterogeneous pore distribution

Different from molding methods, layer-by-layer deposition during the extrusion-printing process directly results in heterogeneous pore distribution in pre-sintered 'brown' parts. The internal structure of such porous materials could be associated with anisotropic shrinkage, which will be discussed in this section.

The microstructures of specimen at various PDS stages along the building direction are characterized, as shown in Fig. 9. The highly porous channels between layers are caused by the inherent trajectories during the printing process. With the binder removal after debinding, these interlayer trajectories will be transformed into small pores, where the increased interlayer lines weaken the bonding effect. Those pores will exhibit a 'micropore coalescence' phenomenon at high temperature, as illustrated by Fig. 10. It appears that the pores inside the printing layers tend to merge generating a larger porous area between the printing layers during the sintering process. These porous areas could further promote atomic diffusion of interlayer particles, accelerating the densification along the building direction and creating anisotropy. Therefore, the sintering anisotropic shrinkage could be caused by the inhomogeneous initial pore distribution due to interlayer porous structures. The distribution and architecture of these intrinsic porosity areas generated between the printing layers will also vary with different in-plane filling strategies.

In addition to the alternating 45° filling strategy applied in the previous section, the commonly used filling strategy settings for printing process of cube specimens are also divided into 0°/90° reciprocating filling strategies, as illustrated in Fig. 11. For these two filling strategies, in addition to the interlayer porous channels along the building direction, the triangular areas formed during the filament repeated filling process along the orthogonal in-plane directions are also inherent

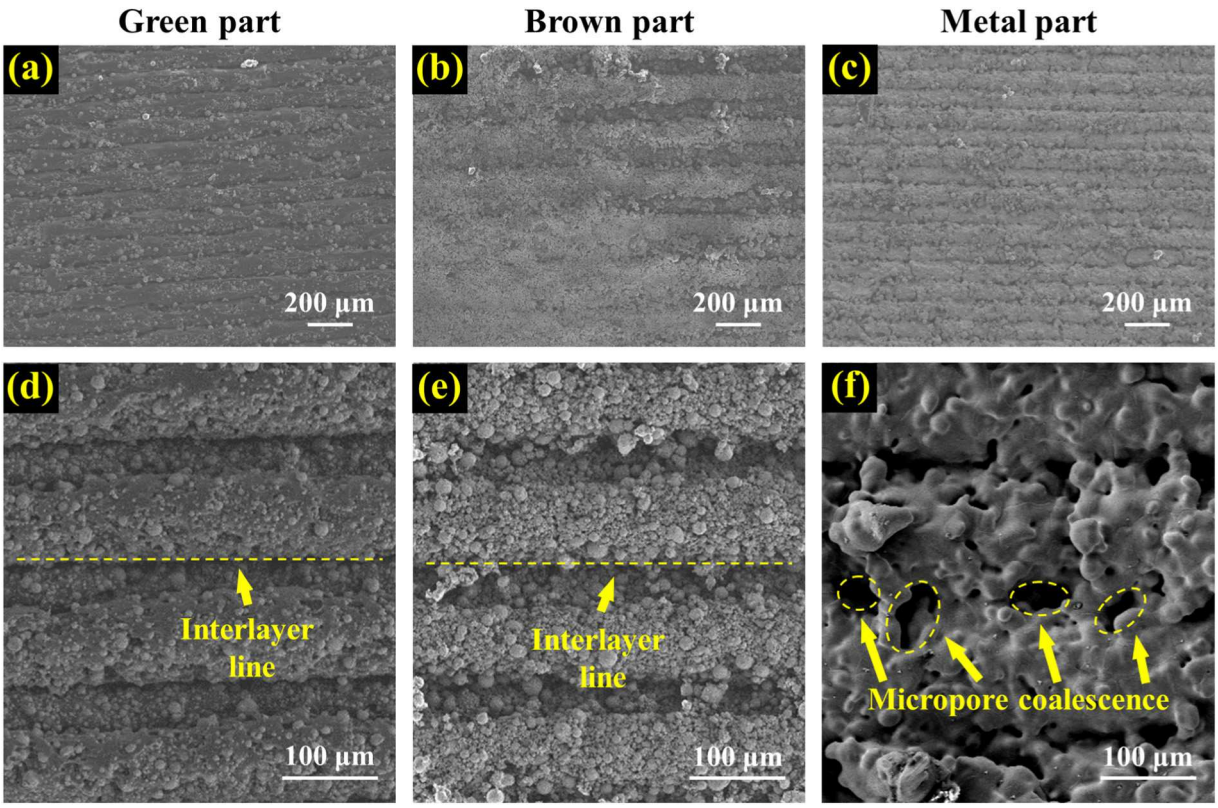

Fig. 9. SEM images of SS 316L specimens at different magnifications: **(a) (d)** printed 'green' part, **(b) (e)** debound 'brown' part, and **(c) (f)** sintered metal part.

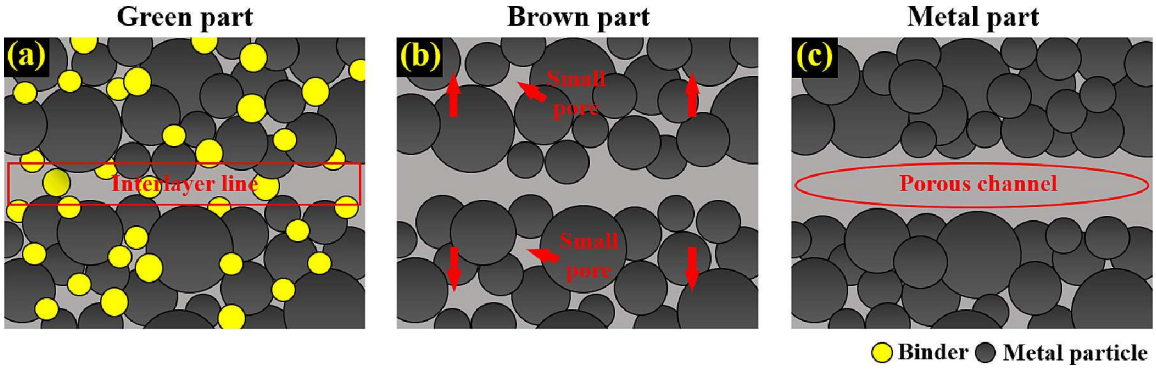

Fig. 10. Illustration of the micropore coalescence phenomenon.

defective areas in the extrusion-printing process. Such triangular areas surrounded by the bending points are distributed in a single orientation of the specimens in the XY orthogonal plane under 0°/90° filling strategies. Such defects are not produced when parallel to the filament filling direction. On the contrary, the vertical direction can be approximated as a superposition of multiple bending points, resulting in a great number of defects along this direction. Such defects can also be analogous to 'interlayer pores' (Y-Z cross section in Fig. 11(b)) along the building direction, which will affect the particle arrangement form along the orthogonal in-plane directions. In other words, for 0°/90° reciprocating filling strategy, the metal particle arrangement form along the orthogonal in-plane direction is similar to that along the building direction. These defective areas may not completely disappear with the lack of pores after sintering.

From the above analysis, the anisotropic shrinkage in PDS is strongly related to the particle arrangement condition. The final dimensional deviation caused by anisotropic shrinkage can potentially affect the dimensional accuracy of components in industrial applications. Therefore, the internal structures of the pre-sintered cube specimens under different filling strategies need to be fully characterized.

Gray-scale images of 2D slices along three directions of pre-sintered cube specimens under different filling strategies are obtained, as displayed in Fig. 12. The gray image is segmented by binarization to divide the pore part and solid part. VG Studio Max is used for 3D volume rendering and reconstruction, where the red and gray regions represent the pores and solid phases, respectively. The pore structure can be eventually extracted.

The specimens printed with different filling strategies are sliced along the XY plane, XZ plane, and YZ plane, respectively. The number of slices in each direction is 886, and the slice thickness is about 10 μm. The pore volume fractions of each slice along each direction are calculated, as displayed in Fig. 13. The specimen printed by alternating 45° filling strategy presents a grid shape pore distribution with interleaved connections. Although there are more interlayer lines along the building

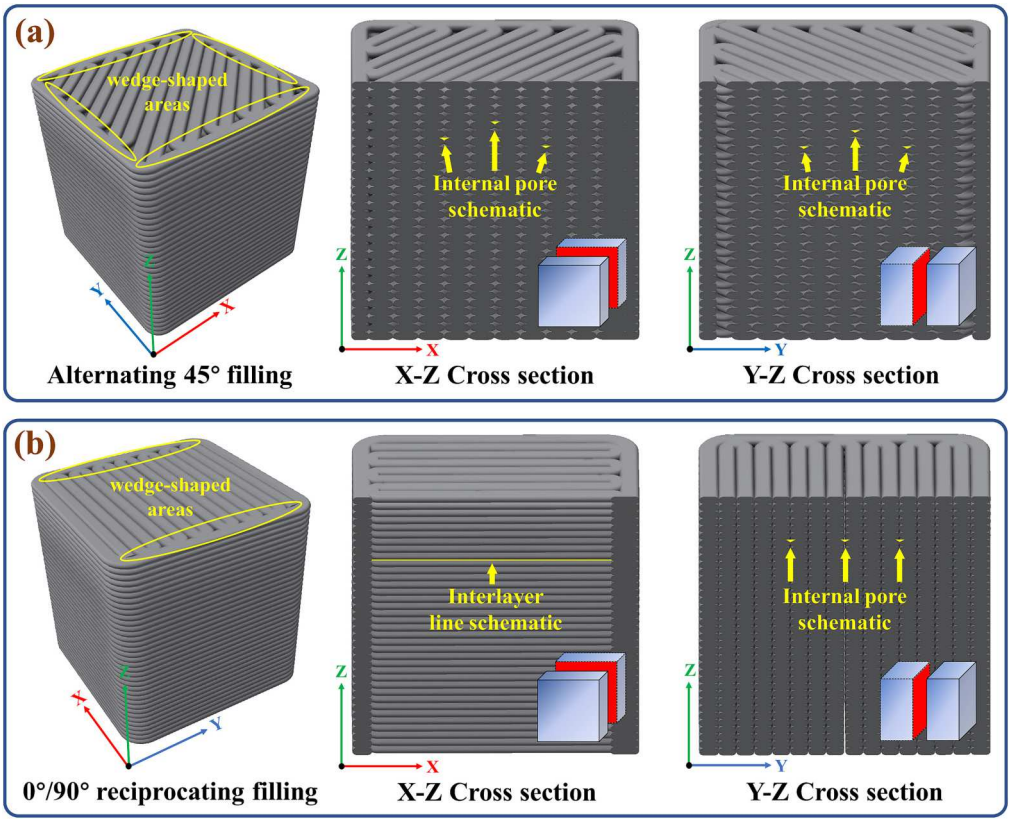

Fig. 11. Schematic of filling strategy used for printing process: **(a)** alternating 45° filling, and **(b)** 0°/90° reciprocating filling.

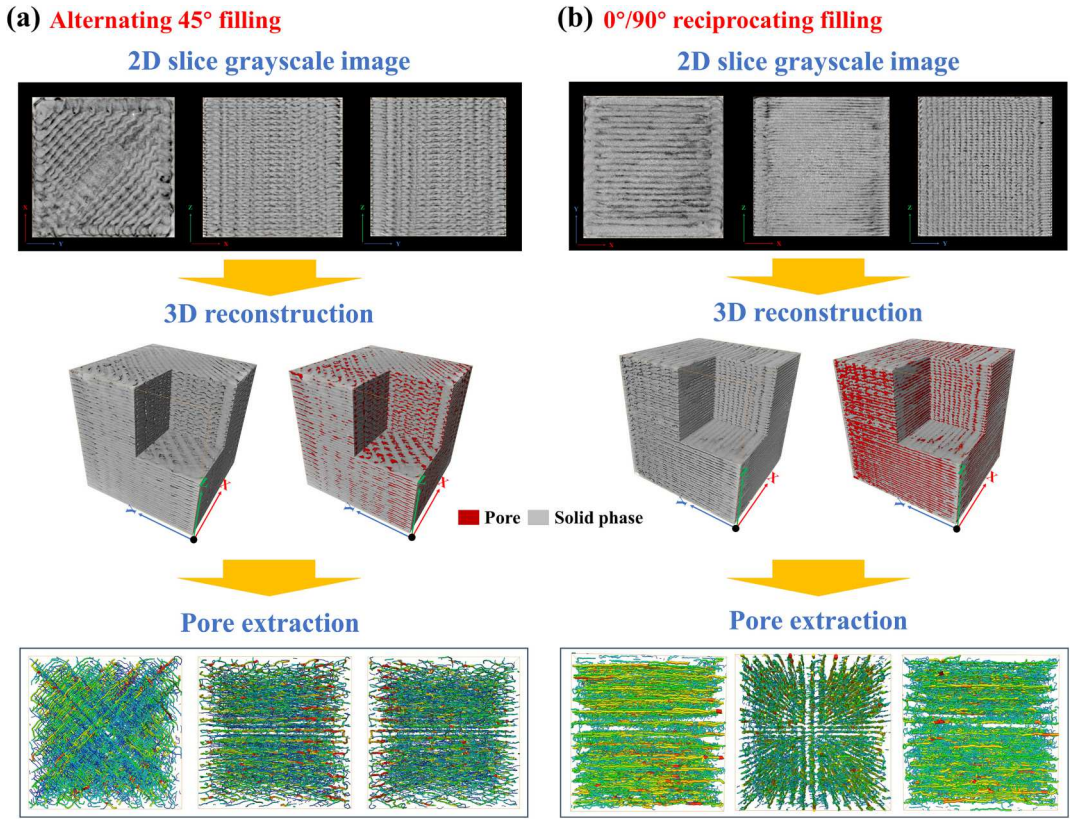

Fig. 12. Pore extraction process of pre-sintered 'brown' part: **(a)** alternating 45° filling, **(b)** 0°/90° reciprocating filling.

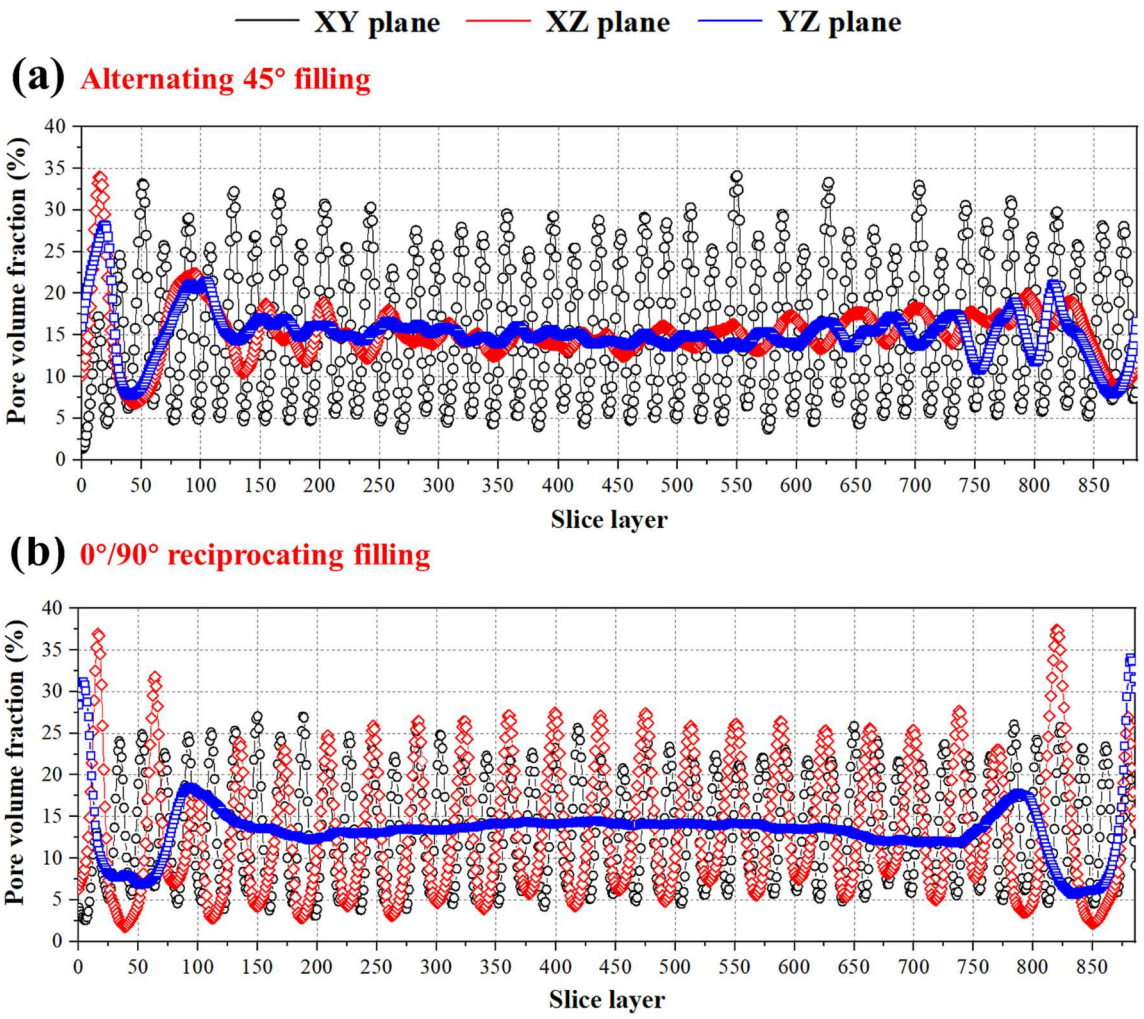

Fig. 13. Pore volume fraction distribution after slicing along XY, XZ, and YZ plane: **(a)** alternating 45° filling, **(b)** 0°/90° reciprocating filling.

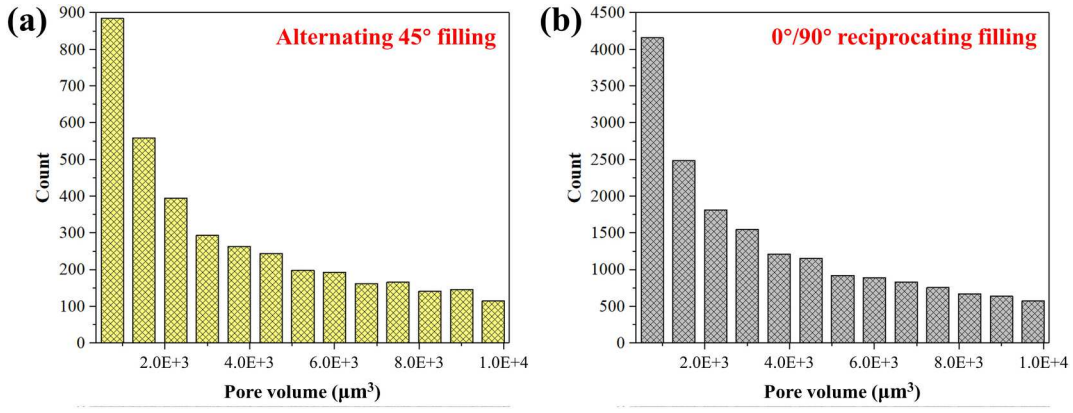

Fig. 14. Histogram for counting the pore size number under two filling strategies: **(a)** alternating 45° filling, **(b)** 0°/90° reciprocating filling.

direction, it is obvious from the pore images of XZ plane and YZ plane that the pore distribution is relatively uniform. The average pore volume fraction of each layer section along the XZ and YZ planes is stable at 15 %. For 0°/90° reciprocating filling strategy, the pores of the specimen are distributed in the direction parallel to the filament filling, which is characterized by non-uniform pore distribution. Specifically, the pore distribution along the XZ plane is similar to that of the XY plane, mostly in the form of interlayer lines. This type of "interlayer lines" are mostly irregular fine filamentous pores, with the pore volume fraction of each layer oscillating between 5 % and 25 %.

Pore sphericity ϕ is introduced to further quantify pore morphology, as expressed by [48]:

$$\phi = \frac{\sqrt[3]{\pi(6V_p)^2}}{A_p} \tag{5}$$

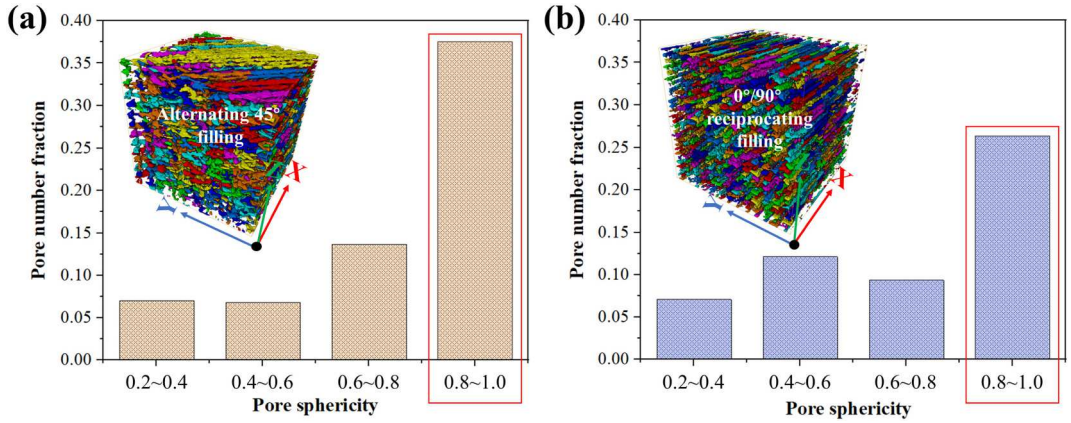

Fig. 15. Statistical results of pore sphericity under two filling strategies: **(a)** alternating 45° filling, **(b)** 0°/90° reciprocating filling.

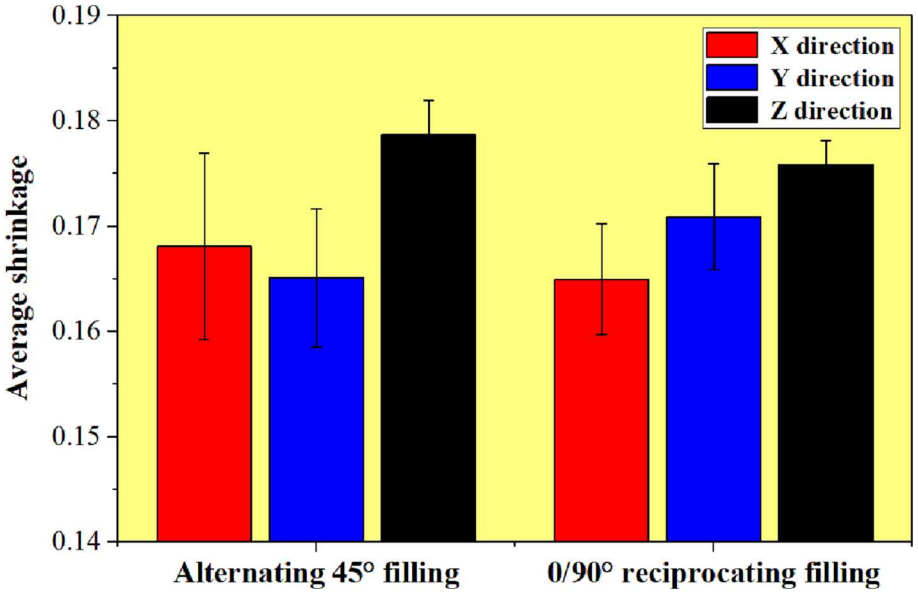

Fig. 16. Results of average size shrinkage for specimens in various filling strategies.

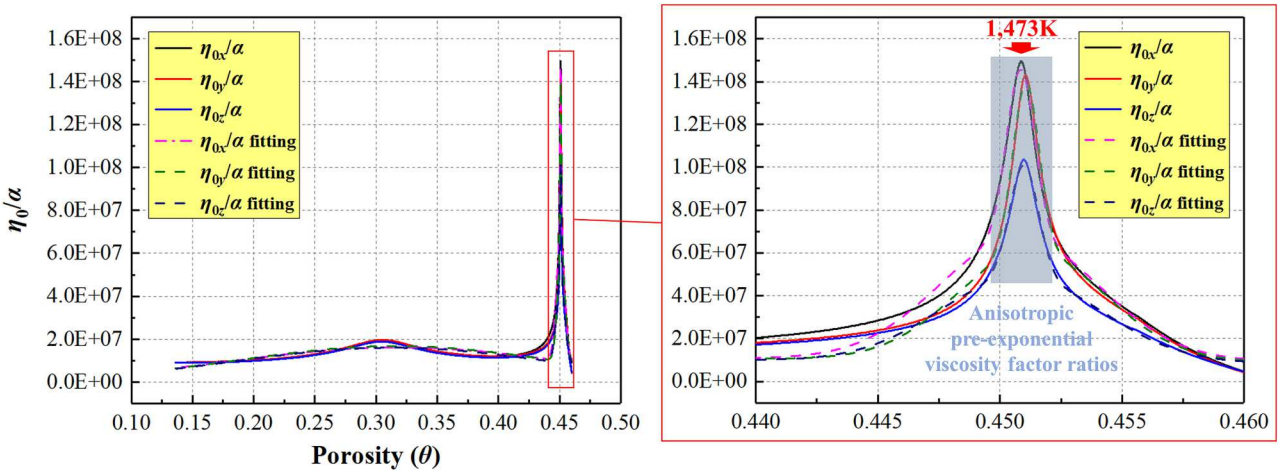

Fig. 17. Extraction of pre-exponential factor ratios and corresponding fitting functions.

where V_p is pore volume, and A_p is pore surface area. If the pore shape approaches to a sphere, the sphericity value is closer to 1, which can be used as a standard to describe the pore shape inside the specimen. As shown in Fig. 14, the number of pores of different sizes with these two filling strategies is counted, respectively. For 0°/90° reciprocating filling strategy, the number of pores of the maximum size is >4000, which is about 4 times that of the alternating 45° filling strategy. The pore surface area is obtained by counting the total area of two-dimensional pores in each slice. Fig. 15 shows the proportion of pores with different ϕ values under two filling strategies. It can be seen that the porosity ratio is higher than 35 % when the pore sphericity ranges from 0.8 to 1 under the alternating 45° filling strategy, while the corresponding ratio is only 25 % under the 0°/90° reciprocating filling strategy. When the pore sphericity ranges from 0.2 to 0.6, the ratio of 0°/90° reciprocating filling strategy is yet significantly higher than that of alternating 45° filling strategy. This proves that a large number of large-size interlayer lines are formed under 0°/90° reciprocating filling strategy along the XZ and XY plane. In addition, a great number of circular/square pores formed by the in-plane extrusion-filling of filament are found along the YZ plane. Therefore, the large number of interlayer lines in this type of filling mode could directly lead to more large-size pores.

The results above fully indicate that the initial pore distribution in pre-sintered 'brown' parts is highly dependent on the filling strategy. Under these two filling strategies and the sintering temperature curve in Fig. 5, 20 cube specimens are printed, debound, and sintered, respectively. The average size shrinkages along the X, Y, and Z directions are calculated, as displayed in Fig. 16. As expected, the three-directional size variations of the sintered specimens under alternating 45° filling strategy are basically consistent with the dilatometry test results. For 0°/90° reciprocating filling strategy, the large-size interlayer lines of the specimen along Y and Z directions correspond to higher shrinkages. The number of printing layers along the Z direction is slightly higher than that of reciprocating filling tracks along the Y direction, showing a higher shrinkage along Z direction. Conversely, the specimen has lower porosity along the direction parallel to the filament filling, and thus exhibits lower shrinkage. In addition, it can also be found that the sintered specimen under alternating 45° filling strategy has a higher shrinkage along the Z direction and exhibits stronger anisotropy. This can be explained by the larger interlayer gap formed by alternating lapping between filaments, as demonstrated by Fig. 13. At the same time, larger deformation also potentially increases the manual measurement error.

4.3. Anisotropic viscous behavior

In our previous model, the fitting result of viscosity pre-exponential factor were found to be nonlinear. Herein, we decipher the connections among pore distribution of heterogeneous porous materials and anisotropic shrinkage. With a heterogeneous pore distribution, viscous behavior along X, Y, and Z directions could be anisotropic. Thus, the anisotropic viscosity parameters can be expressed below (the expression in X direction only is selected for illustration purpose):

$$\eta_x = \frac{-3\alpha(1-\theta)^2}{2r\left(\left(\psi+\frac{2}{3}\varphi\right)\dot{e}_x+\left(\psi-\frac{\varphi}{3}\right)\dot{e}_y+\left(\psi-\frac{\varphi}{3}\right)\dot{e}_z\right)} = \eta_{0x}exp\left(\frac{Q_x}{RT}\right) \tag{6}$$

The sintering of porous materials is a dynamic evolution of porosity. Here, the shear modulus φ and bulk modulus ψ are affected by the porosity θ [41]. To understand the relationship between sintering anisotropy and porosity, we eliminate the specific surface energy α and obtain the pre-exponential factor ratio, η_{0x}/α in X direction:

$$\frac{\eta_{0x}}{\alpha} = \frac{-3(1-\theta)^2}{2rexp\left(\frac{Q_x}{RT}\right)\left(\left(\psi+\frac{2}{3}\varphi\right)\dot{e}_x+\left(\psi-\frac{\varphi}{3}\right)\dot{e}_y+\left(\psi-\frac{\varphi}{3}\right)\dot{e}_z\right)} \tag{7}$$

Using the densification data (θ, $\dot{e}_x$, $\dot{e}_y$, $\dot{e}_z$, r) combined with the viscosity activation energies (Q_x, Q_y, and Q_z) [41], η_{0x}/α can be calculated. Meanwhile, η_{0y}/α, and η_{0z}/α can also be obtained in the same way. All three pre-exponential factor ratios are displayed in Fig. 17, which can be considered as a function between η_0/α and θ. The mathematically quantified relationship between the pre-exponential factors and porosity can be found in Appendix A.

The difference of pre-exponential factor ratios in three directions for porosity values from 0.42 to 0.46 indicates a higher level of anisotropy at the beginning of sintering and peaks at 1473 K (which also validates the results in Section 4.1). Then, with the specimen shrinkage and pore elimination, three curves are virtually converged, indicating that the specimen tends to be isotropic during the final sintering stage. Although porosity values cannot fully describe heterogeneous porous materials, especially the pre-sintered 'brown' parts. The dynamic evolution of pore distribution during sintering process can be linked to the anisotropic viscosity pre-exponential ratios. The lower value in Z direction (η_{0z}/α) could be related to the formation of interlayer pores after layer-by-layer deposition, which can be interpreted as the lower viscous resistance accelerating the atomic diffusion between printing layers. Therefore, it can be concluded that the formation and attenuation of the anisotropy shrinkage phenomenon are highly dependent on the evolution of anisotropic viscous behavior.

5. Conclusions and future direction

In this work, the mesoscale sintering behavior during the material extrusion-based AM process of SS 316L were comprehensively revealed. Based on the three-dimensional dilatometry experimental results, X-ray computed tomography, and theoretical analysis, the complex sintering shrinkage behavior during the Printing-Debinding-Sintering (PDS) process were fully investigated. The findings in this work resulted in the following conclusions:

(1) Based on the alternating 45° filling method used in dilatometry test, the Z direction showed a higher sintering shrinkage and the X and Y directions exhibited similar shrinkage behaviors. The results of anisotropy factor indicated that the formation and reduction of anisotropic shrinkage are separated by 1473 K. The second increase of shrinkage rate could be explained as the formation of body centered cubic phase (δ-ferrite) at high temperature.
(2) With the removal of the polymer in filament after debinding, the interlayer micropores during the printing process generated a pore coalescence phenomenon at high temperature stages. These areas with larger porosities formed porous channels and represented a non-uniform pore distribution.
(3) The sintering process in PDS could be associated with the pore structure in pre-sintered 'brown' parts, which is highly dependent on the filling strategy. Different filling strategies changed the particle arrangement form of porous body after debinding, resulting in the variation of initial pore distribution.
(4) The anisotropic shrinkage during PDS process was first attributed to the difference of anisotropic viscosity pre-exponential factor ratios along each direction caused by the non-uniform pore distribution. With the elimination of pores at high temperature stages, the anisotropic viscous behavior gradually tended to be isotropic.

Our findings have suggested that the anisotropic shrinkage behavior during PDS is attributed to the initial pore distribution, closely related to the print parameters. To obtain a nearly dense metal part with quasi-isotropic shrinkage at three directions, an appropriate range of layer thickness would be manipulated to obtain a uniform initial pore distribution in the future work.

Declaration of competing interest

The authors declare that they have no known competing financial interests or personal relationships that could have appeared to influence the work reported in this paper.

Acknowledgment

Fuda Ning would like to acknowledge the support from the U.S. National Science Foundation through award (CMMI-2224309) as well as the grant (#ADLG241) from Small Scale Systems Integration and Packaging (S^3IP) Center of Excellence, funded by New York Empire State Development's Division of Science, Technology and Innovation. Fuji Wang appreciates the support from Liaoning Revitalization Talents Program (Grant No. XLYC1801008, XLYCYSZX1901, and XLYC1902014), Science and Technology Innovation Foundation of Dalian (Grant No. 2019CT01).

Appendix A. Three-directional pre-exponential factor ratios

The three-directional pre-exponential factor ratios as a function of porosity is shown as follows:

$$\frac{\eta_{0x1}}{\alpha} = 7.845E7exp(-((\theta-0.55)/0.0008))^2 + 1.626E7exp(-((\theta-0.42)/0.192))^2 + 5.703E7exp(-((\theta-0.55)/0.0046))^2 \quad (A.1)$$

$$\frac{\eta_{0y1}}{\alpha} = 7.854E7exp(-((\theta-0.55)/0.00076))^2 + 1.683E7exp(-((\theta-0.42)/0.184))^2 + 5.084E7exp(-((\theta-0.55)/0.0043))^2 \quad (A.2)$$

$$\frac{\eta_{0z1}}{\alpha} = 5.227E7exp(-((\theta-0.55)/0.00084))^2 + 1.609E7exp(-((\theta-0.41)/0.182))^2 + 3.944E7exp(-((\theta-0.55)/0.0047))^2 \quad (A.3)$$

References

[1] Gao C, Wolff S, Wang S. Eco-friendly additive manufacturing of metals: energy efficiency and life cycle analysis. J Manuf Syst 2021;60:459–72. https://doi.org/10.1016/j.jmsy.2021.06.011.
[2] Do T, Kwon P, Shin CS. Process development toward full-density stainless steel parts with binder jetting printing. Int J Mach Tools Manuf 2017;121:50–60. https://doi.org/10.1016/j.ijmachtools.2017.04.006.
[3] Kurose T, Abe Y, Santos MVA, Kanaya Y, Ishigami A, Tanaka S, et al. Influence of the layer directions on the properties of 316L stainless steel parts fabricated through fused deposition of metals. Mater 2020;13:2493. https://doi.org/10.3390/ma13112493.
[4] Li H, Liu Y, Liu Y, Zeng Q, Hu K, Lu Z, et al. Effect of debinding temperature under an argon atmosphere on the microstructure and properties of 3D-printed alumina ceramics. Mater Charact 2020;168:110548. https://doi.org/10.1016/j.matchar.2020.110548.
[5] Wakai F, Akatsu T. Anisotropic viscosities and shrinkage rates in sintering of particles arranged in a simple orthorhombic structure. Acta Mater 2010;58:1921–9. https://doi.org/10.1016/j.actamat.2009.11.035.
[6] Raj PM, Odulena A, Cannon WR. Anisotropic shrinkage during sintering of particle-oriented systems: numerical simulation and experimental studies. Acta Mater 2002;50:2559–70. https://doi.org/10.1016/S1359-6454(02)00083-6.
[7] Shui A, Kato Z, Tanaka S, Uchida N, Uematsu K. Sintering deformation caused by particle orientation in uniaxially and isostatically pressed alumina compacts. J Eur Ceram Soc 2002;22:311–6. https://doi.org/10.1016/S0955-2219(01)00292-8.
[8] Shui A, Zeng L, Uematsu K. Relationship between sintering shrinkage anisotropy and particle orientation for alumina powder compacts. Scr Mater 2006;55:831–4. https://doi.org/10.1016/j.scriptamat.2006.07.026.
[9] Lu K, Hiser M, Wu W. Effect of particle size on three dimensional printed mesh structures. Powder Technol 2009;192:178–83. https://doi.org/10.1016/j.powtec.2008.12.011.
[10] Biswas S, Schwen D, Wang H, Okuniewski M, Tomar V. Phase field modeling of sintering: role of grain orientation and anisotropic properties. Comput Mater Sci 2018;148:307–19. https://doi.org/10.1016/j.commatsci.2018.02.057.
[11] Shang H, Mohanram A, Olevsky EA, Bordia RK. Evolution of anisotropy in hierarchical porous ceramics during sinter-forging. J Eur Ceram Soc 2016;36:2937–45. https://doi.org/10.1016/j.jeurceramsoc.2015.12.042.
[12] Zavaliangos A, Missiaen JM, Bouvard D. Anisotropy in shrinkage during sintering. Sci Sinter 2006;38:13–25. https://doi.org/10.2298/SOS0601013Z.
[13] Kanchika S, Wakai F. Surface tension-pressure superposition principle for anisotropic shrinkage of an ellipsoidal pore in viscous sintering. J Eur Ceram Soc 2018;38:4283–9. https://doi.org/10.1016/j.jeurceramsoc.2018.05.015.
[14] Manière C, Olevsky EA. Porosity dependence of powder compaction constitutive parameters: determination based on spark plasma sintering tests. Scr Mater 2017;141:62–6. https://doi.org/10.1016/j.scriptamat.2017.07.026.
[15] Olevsky EA, Molinari A. Instability of sintering of porous bodies. Int J Plast 2000;16:1–37. https://doi.org/10.1016/S0749-6419(99)00032-7.
[16] Green DJ, Guillon O, Rödel J. Constrained sintering: a delicate balance of scales. J Eur Ceram 2008;28:1451–66. https://doi.org/10.1016/j.jeurceramsoc.2007.12.012.
[17] Bordia RK, Zuo R, Guillon O, Salamone SM, Rödel J. Anisotropic constitutive laws for sintering bodies. Acta Mater 2006;54:111–8. https://doi.org/10.1016/j.actamat.2005.08.025.
[18] Lichtner A, Roussel D, Röhrens D, Jauffres D, Villanova J, Martin CL, et al. Anisotropic sintering behavior of freeze-cast ceramics by optical dilatometry and discrete-element simulations. Acta Mater 2018;155:343–9. https://doi.org/10.1016/j.actamat.2018.06.001.
[19] Wakai F, Shinoda Y. Anisotropic sintering stress for sintering of particles arranged in orthotropic symmetry. Acta Mater 2009;57:3955–64. https://doi.org/10.1016/j.actamat.2009.04.049.
[20] Alvarado-Contreras JA, Olevsky EA, German RM. Modeling of gravity-induced shape distortions during sintering of cylindrical specimens. Mech Res Commun 2013;50:8–11. https://doi.org/10.1016/j.mechrescom.2013.02.007.
[21] Olevsky EA, Shoales GA, German RM. Temperature effect on strength evolution under sintering. Mater Res Bull 2001;36:449–59. https://doi.org/10.1016/S0025-5408(01)00523-2.
[22] Wonisch A, Guillon O, Kraft T, Moseler M, Riedel H, Rödel J. Stress-induced anisotropy of sintering alumina: discrete element modelling and experiments. Acta Mater 2007;55:5187–99. https://doi.org/10.1016/j.actamat.2007.05.038.
[23] Jiang D, Ning F. Additive manufacturing of 316L stainless steel by a printing-debinding-sintering method: effects of microstructure on fatigue property. J Manuf Sci E T ASME 2021;143:091007. https://doi.org/10.1115/1.4050190.
[24] Gonzalez-Gutierrez J, Arbeiter F, Schlauf T, Kukla C, Holzer C. Tensile properties of sintered 17-4PH stainless steel fabricated by material extrusion additive manufacturing. Mater Lett 2019;248:165–8. https://doi.org/10.1016/j.matlet.2019.04.024.
[25] Gong HJ, Snelling D, Kardel K, Carrano A. Comparison of stainless steel 316L parts made by FDM- and SLM-based additive manufacturing processes. Miner Met Mater Ser 2019;71:880–5. https://doi.org/10.1007/s11837-018-3207-3.
[26] Quarto M, Carminati M, D'Urso G. Density and shrinkage evaluation of AISI 316L parts printed via FDM process. Mater Manuf Process 2020;36:1535–43. https://doi.org/10.1080/10426914.2021.1905830.
[27] Rosnitschek T, Seefeldt A, Alber-Laukant B, Neumeyer T, Altstädt V, Tremmel S. Correlations of geometry and infill degree of extrusion additively manufactured 316L stainless steel components. Mater 2021;14:5173. https://doi.org/10.3390/ma14185173.
[28] Obadimu SO, Kourousis KI. Shrinkage behaviour of material extrusion steel 316L: influence of primary 3D printing parameters. Rapid Prototyp J 2022;28:92–101. https://doi.org/10.1108/RPJ-07-2022-0224.
[29] Ait-Mansour I, Kretzschmar N, Chekurov S, Salmi M, Rech J. Design-dependent shrinkage compensation modeling and mechanical property targeting of metal FFF. PIAM 2020;5:51–7. https://doi.org/10.1007/s40964-020-00124-8.
[30] Abe Y, Kurose T, Santos MVA, Kanaya Y, Ishigami A, Tanaka S, et al. Effect of layer directions on internal structures and tensile properties of 17-4PH stainless steel parts fabricated by fused deposition of metals. Mater 2021;14:243. https://doi.org/10.3390/ma14020243.
[31] Rios AC, Hryha E, Olevsky EA, Harlin P. Sintering anisotropy of binder jetted 316L stainless steel: part I – sintering anisotropy. Powder Metall 2021. https://doi.org/10.1080/00325899.2021.2020485.
[32] Li H, Liu Y, Colombo P, Li W, Liu Y, Hu K, et al. The influence of sintering procedure and porosity on the properties of 3D printed alumina ceramic cores. Ceram Int 2021;47:27668–76. https://doi.org/10.1016/j.ceramint.2021.06.191.
[33] Baumgartner S, Gmeiner R, Anna Schönherr J, Stampfl J. Stereolithography-based additive manufacturing of lithium disilicate glass ceramic for dental applications. Mater Sci Eng C 2020;116:111180. https://doi.org/10.1016/j.msec.2020.111180.

[34] Heaney DF, Spina R. Numerical analysis of debinding and sintering of MIM parts. J Mater Process Technol 2007;191:385–9. https://doi.org/10.1016/j.jmatprotec.2007.03.080.
[35] Zhang R, Engel RS, Salamon NJ, German RM. Finite element analysis on the sintering of stainless steel 316L powder compacts. In: Metal powder industries federation. 2002 advances in powder metallurgy and particulate materials; 2002. p. 60–8.
[36] Song J, Gelin JC, Barrière T, Liu B. Experiments and numerical modelling of solid state sintering for 316L stainless steel components. J Mater Process Technol 2006;177:352–5. https://doi.org/10.1016/j.jmatprotec.2006.04.111.
[37] Olevsky EA. Theory of sintering: from discrete to continuum. Mater Sci Eng R Rep 1998;23:41–100. https://doi.org/10.1016/S0927-796X(98)00009-6.
[38] McMeeking RM, Kuhn LT. A diffusional creep law for powder compacts. Acta Metall Mater 1992;40:961–9. https://doi.org/10.1016/0956-7151(92)90073-N.
[39] German RM. Strength evolution in debinding and sintering. In: Proceedings of 3nd international conference on the science, Technology & applications of sintering. Pennsylvania; 2003. p. 1–13.
[40] Kraft T, Riedel H. Numerical simulation of solid state sintering; model and application. J Eur Ceram 2004;24:345–61. https://doi.org/10.1016/S0955-2219(03)00222-X.
[41] Jiang D, Ning F. Anisotropic deformation of 316L stainless steel overhang structures built by material extrusion based additive manufacturing. Addit Manuf 2022;50:102545. https://doi.org/10.1016/j.addma.2021.102545.
[42] Liu B, Wang Y, Lin Z, Zhang T. Creating metal parts by fused deposition modeling and sintering. Mater Lett 2019;263:127252. https://doi.org/10.1016/j.matlet.2019.127252.
[43] Askari A, Alaei MH, Nekouee K, Omrani AM, Park SJ. The effect of debinding and sintering parameters on the mechanical and microstructural properties of Fe-2Ni metal injection molded compacts. Mater Res Express 2019;6:1165e8. https://doi.org/10.1088/2053-1591/ab4f26.
[45] Liu ZY, Loh NH, Khor KA, Tor SB. Sintering activation energy of powder injection molded 316L stainless steel. Scr Mater 2001;44:1131–7. https://doi.org/10.1016/S1359-6462(01)00664-9.
[46] Reiterer MW, Ewsuk KG, Arguello JG. An Arrhenius-type viscosity function to model sintering using the skorohod-olevsky viscous sintering model within a finite element code. Am Ceram Soc 2006;89:1930–5. https://doi.org/10.1111/j.1551-2916.2006.01041.x.
[47] Lecis N, Mariani M, Beltrami R, Emanuelli L, Casati R, Vedani M, et al. Effects of process parameters, debinding and sintering on the microstructure of 316L stainless steel produced by binder jetting. Mater Sci Eng A 2021;828:142108. https://doi.org/10.1016/j.msea.2021.142108.
[48] Zhou H, Zhou M, Cheng M, Guo X, Li Y, Ma P, et al. High resolution X-ray microtomography for the characterization of pore structure and effective thermal conductivity of iron ore sinter. Appl Therm Eng 2017;127:508–16. https://doi.org/10.1016/j.applthermaleng.2017.08.051.